PERGAMON

International Journal of Heat and Mass Transfer 44 (2001) 2917–2932

International Journal of HEAT and MASS TRANSFER

www.elsevier.com/locate/ijhmt

Applying heat–entropy analogies with experimental study of interface tracking in phase change heat transfer

G.F. Naterer *

University of Manitoba, Department of Mechanical and Industrial Engineering, 15 Gillson Street, Winnipeg, Manitoba, Canada R3T 2N2

Received 27 March 2000; received in revised form 30 August 2000

Abstract

Heat–entropy analogies are applied to problems involving phase change heat transfer with fluid flow. In the experimental studies, entropy is not measured directly, but temperature and other measurements yield associated entropy results for improved understanding of the phase change processes. The entropy-based framework is shown to serve an important role in modelling of momentum phase interactions and thermal recalescence, as well as numerical stability in the computations. Numerical and experimental results indicate that entropy can serve as an effective variable in describing and predicting various interfacial processes during phase change. © 2001 Elsevier Science Ltd. All rights reserved.

1. Introduction

Due to the importance of solid–liquid phase change in various applications (i.e. materials processing, ice accretion on structures, thermal energy storage in electronic assemblies), extensive research has examined interface tracking during phase change. Previous experimental studies on solidification and melting have often employed aqueous mixtures such as sodium chloride–water [1] and ammonium chloride–water [2], due to their translucency, low melting temperatures and similarity with respect to dendritic solidification in metals. Important transport processes have been observed in these studies, including dendritic formations [2] and planar interface movement [3]. Furthermore, recent studies have examined the potential benefits of microgravity solidification processing. For example, Cahoon et al. [4] have observed different microstructures during microgravity solidification, in comparison to similar conditions in unit gravity, as a result of lower dendrite growth velocities (i.e. no convective mixing) in the microgravity ingots.

The primary difficulties in accurate interface tracking are the typically unknown position of the phase interface(s) and the influence of interdendritic flow on its movement. Modelling of solidification shrinkage, due to differences in density between solid and liquid phases, can be handled by a simultaneous pressure–velocity coupling in the two-phase zone [5]. Pockets or channels of liquid are entrapped within the solid matrix during dendritic solidification. Recent advances have incorporated the anisotropic characteristics of the two-phase permeability to properly accommodate this momentum transport [6]. Furthermore, Clyne and Kurz [7] assess the role of rapid interface movement on the equilibrium conditions at the phase interface. Additional research innovations have identified the simultaneous processes of momentum and solute transport at the moving phase interface [8]. Both numerical studies (i.e. PHASES algorithm) and experimental studies of these processes have been conducted by Naterer and Schneider [9,10]).

Experimental studies of interface tracking often involve temperature and/or fluid velocity measurements, together with photographic observations of the interface characteristics and motion during phase change. During solidification processes, an observer may anticipate a gradual temperature decline in the fluid as a result of external cooling. However, additional phenomena, including recalescence (temperature rise corresponding to

* Tel.: +1-204-474-9805; fax: +1-204-275-7507.
E-mail address: naterer@cc.umanitoba.ca (G.F. Naterer).

PII: S0017-9310(00)00296-9

Nomenclature

C	solute concentration (pct.weight)
Δe_f	heat of fusion (J/kg)
Fo	Fourier modulus ($=\alpha t/Y^2$)
k	thermal conductivity (W/m K)
t	time (s)
T	temperature (K)
Y	domain height (m)

Greek symbols

α	thermal diffusivity (m^2/s)
μ	viscosity (kg/m s)
ρ	density (kg/m^3)

Subscripts

l	liquid
s	solid
0	initial

release of latent heat from freezing crystal), may arise. Recent studies have investigated these detailed thermal conditions, including local reheating during solidification [11]. Due to the numerous unresolved questions regarding transport processes during phase transition, such as conditions leading to recalescence, there remains a strong need for further experimental studies of these processes.

In addition, despite the recent advances in understanding of phase change heat transfer, few studies have considered the detailed significance of entropy transport during the phase transition processes. Recent studies by Naterer have utilized entropy in discrete modelling of phase change [12,13] and fluid flow [14]. Despite the potential importance of the second law of thermodynamics in many applications, three main difficulties have stalled the progress of entropy developments: (i) difficulty in measuring entropy directly (unlike energy, or temperature, and other conserved variables), (ii) inequality (second law) rather than equality (conservation equations) and (iii) entropy de-coupling from energy, solute concentration and momentum equations. As a result, rapid advances involving phase change heat transfer with fluid flow have appeared during recent years despite only a sparse treatment of thermal irreversibility and entropy.

However, consideration of entropy can provide an important mechanism for further understanding of many practical problems such as defect formations in casting or extrusion applications. For example, material defects may include porosity, or non-uniform dispersion of alloy constituents (called macrosegregation). The microstructures and morphological stability of the phase interface are dependent on the molecular disorder at the interface (i.e. entropy transport). The degree of entropy change between solid and liquid phases affects molecular disorder and properties of the solidified material.

In many instances, entropy transport may give deep insight into various fundamental processes during solidification of materials. In order to further appreciate this potential insight, consider several specific applications where entropy mechanisms may provide key details in the understanding of specific material processes. For example, further understanding of oxidation phenomenon can be achieved by observing how manganese precipitates grow on an iron surface during solidification. The precipitates exhibit a uniform orientation and atomic order during growth on the iron surface. Entropy transfer appears significant in this situation since it gives a quantitative indication of microscopic disorder during the precipitate formation. Furthermore, it appears important in iron oxide processing since this oxide can have a square symmetry of atoms in the iron surface where the oxide grows. Atomic symmetry and entropy are closely related, and therefore, information about the oxide orientation and entropy can give important clues about what causes corrosion in this material.

An important example involving electronics applications is semiconductor technologies. Concentric hexagonal pits in cadmium sulphide (widely used semiconductor) exhibit a high crystal symmetry. Dislocation defects have been found to adversely affect electrical properties of this semiconductor, i.e., increase/decrease conductivity by 1000–100,000 times. These defects in the crystalline structure may arise from dilute hydrochloric acid deposits on the crystal surface. In terms of entropy transport, dislocation defects could be reduced through minimal entropy production during material formation. Also, phase change materials (PCMs) have been applied to thermal management of electronic assemblies [15]. In this case, the temperature difference between an electronic component and the PCM, ΔT, at a fixed heat transfer rate, Q, is reduced as the entropy production rate, $Q\Delta T/T^2$, is minimized.

Despite the recognized importance and extensive research dealing with the previously mentioned applications, a relative lack of attention has been devoted to the understanding of entropy transport during these processes. In particular, two-phase entropy transport during solidification, including entropy production and entropy of fusion, has received sparse attention. In this paper, experimental studies will be described for studies of heat–entropy analogies. Comparisons between numerical predictions (based on PHASES algorithm [9]) and the experimental results will be presented. Finally, an assessment of the analogies in providing insight into

various transport phenomena during phase transition will be discussed.

2. Heat transfer experiments

Experimental studies of phase change with fluid flow were conducted with a semi-transparent, aqueous mixture in a rectangular enclosure. The experiments consisted of photographic observations of the phase interface motion, and various measurements, including thermocouple measurements, of thermal and dynamic processes during solidification. An ammonium chloride–water (NH_4Cl–H_2O) mixture with a binary eutectic phase diagram, involving previously reported thermophysical properties [6], was investigated in the present work. A range of water compositions between $C_0 = 0.68$ and $C_0 = 0.76$ was investigated. Unlike liquid metals, this mixture's low (room temperature) freezing point and high transmissivity characteristics in the liquid phase permit easy and clear visual examination of the solidification process. Due to its low entropy of fusion, NH_4Cl–H_2O solidifies in a dendritic nature like many binary metal alloys. A freezing material with a low entropy of fusion has a high tendency to incorporate new atoms onto the solid crystals, or dendrite arms, because of small differences in structure and density between the solid and liquid phases.

The rectangular test cell (see Fig. 1(a)) was constructed with brass heat exchanger walls at the side and bottom faces and plexiglass windows on the front, back and top faces. The observation area dimensions (10.16×7.94 cm^2) permitted an adequate clearance between internally placed thermocouples. It was assumed that sufficient cell depth (21.27 cm) was achieved to effectively remove three-dimensional variations of thermal and flow fields along the centre measurement plane (see Appendix A). At the specified cell depth and flow conditions, the ratio between the front and back side frictional forces to the net friction force was approximately 10% in the worst case (initial condition) situation. At subsequent stages of solidification, this ratio was reduced because the exposed liquid area on the observation windows was reduced. Since the front and back frictional forces were sufficiently small in comparison to the side and base wall frictional forces, the internal flow field was considered two-dimensional in character. Visual observations of the solidification processes confirmed these assertions.

The observation windows were designed with double-pane plexiglass with a 9.5 mm thick interior window and a 0.6 mm thick exterior window. An internal 9.5 mm air gap minimized three-dimensional heat transfer effects through the ends of the test cell. It was estimated that the conduction resistance through the side walls was less than 1.0% of the thermal resistance of the front and back plexiglass composite system (see Appendix A). As a result, three-dimensional thermal effects were also considered negligible. The side and bottom brass plates were machined with internal parallel passages to provide uniform coolant flow characteristics through each channel and uniform heat extraction through each plate. Each plate heat exchanger was attached to a thermal bath and control unit through insulated PVC tubing. An antifreeze liquid (ethylene glycol) was used as the coolant. Pressure port and suction port lines from the thermal bath were divided into three distinct lines for each heat exchanger in the test cell (see Fig. 1(a)).

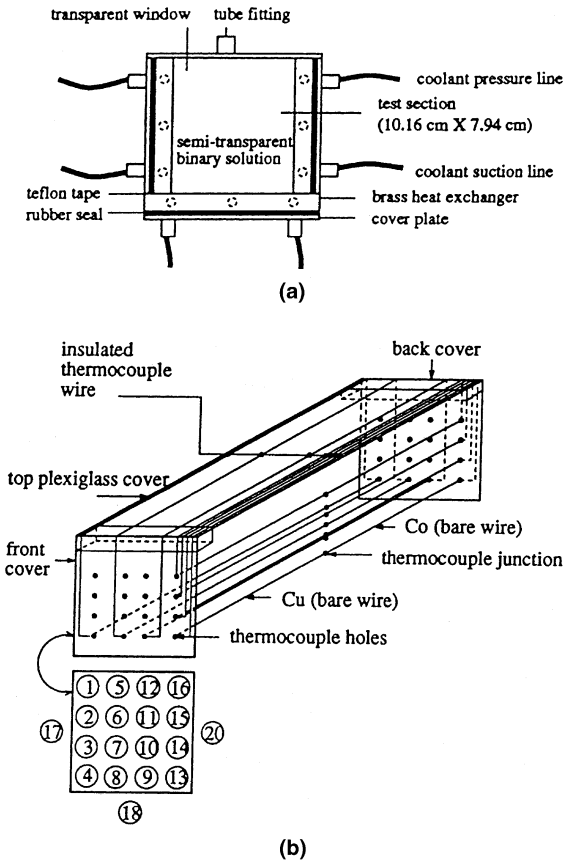

Fig. 1. (a) Experimental test cell and (b) thermocouple grid.

The thermocouple grid consisted of 16 copper–constantan type T, 0.5 mm diameter, bare wire thermocouples soldered at the midplane within a plexiglass frame (see Fig. 1(b)). The thermocouple frame was inserted into the test cell before each simulation. The horizontal locations of each thermocouple column within the grid were 0.64, 2.54, 5.72 and 7.62 cm, respectively. The vertical locations of each thermocouple row within the grid were 0.64, 2.54, 5.08 and 7.62 cm, respectively. Convection and conduction losses down the thermocouple wires were considered negligible (see

Appendix A). Thermocouples were assembled within the cell walls and flow lines to monitor the boundary and system conditions. Side wall midplane temperatures were monitored at heights of 7.62 and 2.54 cm and the base midplane temperatures were monitored at a distance of 2.54 cm from each side wall.

Although entropy is a main focus of this work, it is not measured directly, but rather indirectly, through the above thermocouple measurements. For an incompressible binary component mixture, entropy varies with temperature and concentration, and phase fraction can be estimated based on these two values and the binary phase equilibrium diagram. From the Gibbs equation, it is noted that the entropy change effectively arises from an energy change with respect to temperature and concentration. In the present studies, only the effects of temperature on entropy change will be recorded. In single phase experiments, it has been shown that the remaining Dufour effects due to concentration are typically negligible [16]. During phase transition, the additional entropy change of fusion can be inferred by temperature measurements corresponding with the rate of release (or absorption) of latent heat. As a result, it is anticipated that the current thermocouple measurements can provide the main information regarding entropy change in the current experiments.

In each experiment, the side and base walls were maintained at sub-zero temperature conditions and the top surface was fixed with an insulating cover. Temperature measurements were recorded on a regular basis with a data acquisition system. The system's accuracy with the thermocouple measurements was assessed as ± 0.4 K. Additional errors due to heat losses from the thermocouple junction are assessed in Appendix A. Visual observations were recorded with a Sony handycam recorder and photographed with a Canon AE1 camera. Additional colour photographs of the digital image scans were obtained with a Minolta X-370 camera. Quantitative studies and qualitative (video–photographic) studies were conducted separately to avoid interference between each other. Identical test cases were performed at least twice to confirm repeatable results.

The results from experimental and numerical studies will be presented in the following section. In these studies, heat–entropy analogies will be examined in view of understanding and predicting various interfacial processes during solid–liquid phase change with fluid flow.

3. Applications and results

In the following first problem, numerical studies are compared with experimental data of Yoo and Viskanta [6], whereas the experiments described in the previous section are utilized in the subsequent second problem.

3.1. Problem 1: phase change with single convective cell

In this problem, predictions of binary mixture solid–liquid phase change with free convection in a two-dimensional domain are investigated (see Fig. 2(a)) in conjunction with some heat–entropy analogies. Solidification of an aqueous ammonium chloride solution in a square enclosure (4.7×4.7 cm^2) is examined. This binary solution has a phase equilibrium diagram with eutectic and melting temperatures of $T_e = 258$ K and $T_m = 633.6$ K, respectively. In this problem, the left and right boundaries are maintained at isothermal conditions of $T = 307.5$ K and $T = 253$ K, respectively, and the upper and lower boundaries are well insulated (adiabatic).

The initial water composition was assumed uniform at $C_0 = 0.70$. Thermophysical properties include $\rho = 1112$ kg/m^3, $c_{p,l} = 3249$ J/kg K, $c_{p,s} = 1870$ J/kg K, $k_l = 0.58$ W/m K, $k_s = 0.39$ W/m K, $D = 1.0 \times 10^{-12}$ m^2/s (mass diffusivity), $\Delta e_f = 314$ kJ/kg and $\mu = 1.6 \times 10^{-3}$ kg/m s. Finite element grids and results with 25×25, 30×30 and 40×40 elements are presented and the transient solutions are performed to $t = 2400$ s. The numerical accuracy and performance of the overall formulation, including the impact of various heat–entropy analogies, will be assessed. This assessment involves both grid and time-step sensitivity studies as well as comparisons with experimental data.

Results from the numerical simulations are shown in Figs. 2–4. Fig. 2(b)–(d) shows the isotherms (dimensionless 0.1 increments), liquid fraction contours and velocity vectors at $t = 480$ s, respectively. At this stage of solidification, heat conduction remains dominant in the solid and mushy regions near the right boundary, but a buoyancy-driven recirculation cell distorts the isotherms in the liquid region (see Fig. 2(b) and (d)). In Fig. 2(d), the results illustrate the upward flow near the hot boundary and the downward liquid flow along the colder phase interface. Momentum is transported across the liquidus interface by liquid shear stresses and bulk liquid penetration across the phase interface.

In the finite element computations, numerical iterations are performed within the energy equation (phase–temperature iterations) and between species concentration, fluid flow and energy equations [9]. The phase–temperature iterative rules enforce passage of each finite volume through a two-phase region (thereby experiencing latent heat) and appropriate phase change of neighbouring volumes. It may be shown that these thermal guidelines are essentially discrete analogies of the second law of thermodynamics (type of heat–entropy analogy). In the computations, phase–temperature convergence is typically achieved within 10 iterations; the iterative procedure permits reliable convergence performance while successfully interacting with the phase equilibrium diagram and solute transport equation.

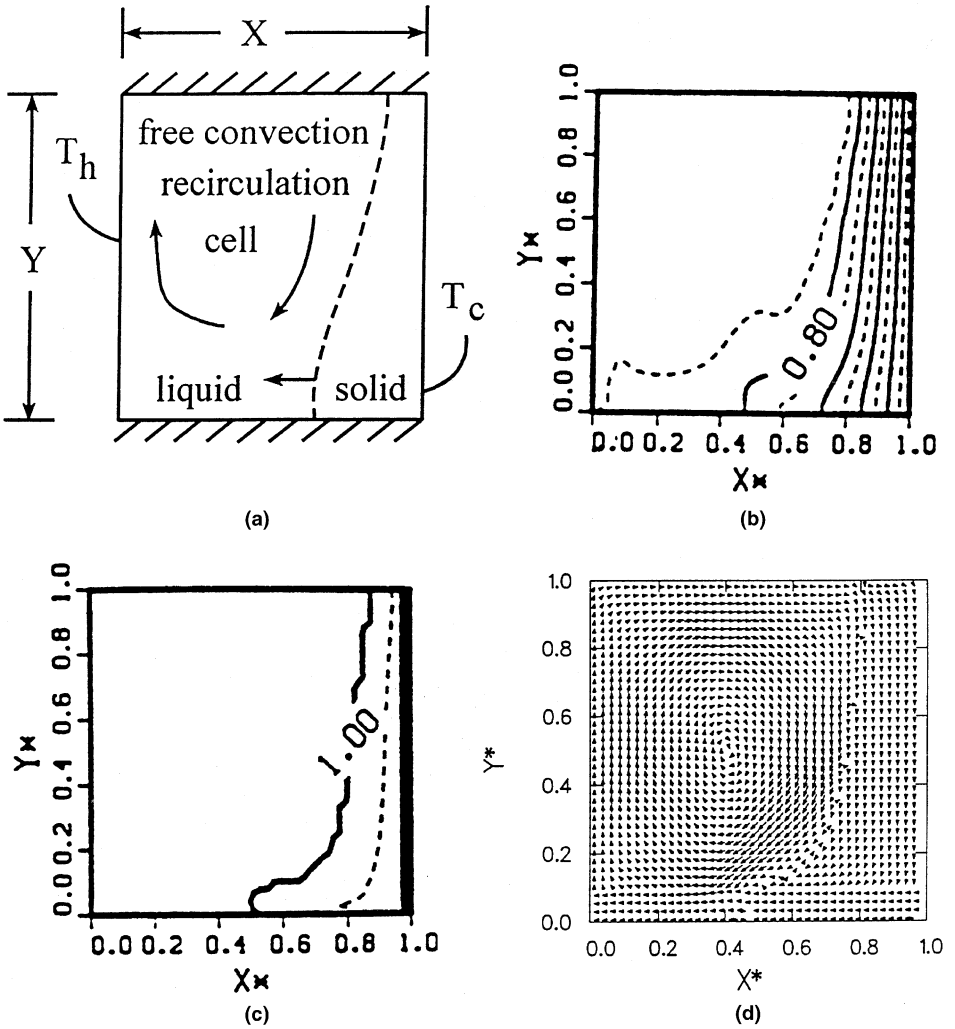

Fig. 2. Problem 1: (a) schematic, (b) isotherms, (c) liquid fraction contours and (d) velocity vectors ($t = 480$ s).

Furthermore, stable inter-equation convergence with the mass and momentum equations was achieved. In conventional iterative techniques, such as Picard iteration, interface tracking is often based on ad hoc convergence tolerances while randomly cycling through tentative phase distributions in many cases. In contrast, the current formulation provides an efficient and physically-based alternative using the second law.

Results at $t = 1200$ s are illustrated in Fig. 3. The recirculating flow (3(c)) further affects the profiles of isotherms (Fig. 3(a)) and liquid fraction contours (Fig. 3(b)). The phase interface profile ($f_l = 1$ contour) shows that convection of cold interdendritic fluid has occurred along the lower boundary. Phase change occurs along the lower boundary due to this convective heat transfer, as well as a reduction of liquidus temperature due to convective transport of solute. On the other hand, upward flow of warmer liquid along the left boundary maintains a liquid region along the top left portion of the cavity.

Fig. 4(a)–(c) illustrate midpoint liquid concentration, temperature profile (along horizontal cavity midplane) and phase interface position, respectively. In Fig. 4(a)–(c), results with the present PHASES algorithm are compared with experimental and computational results of Yoo and Viskanta [6]. Grid refinements with 25×25, 30×30 and 40×40 elements, as well as time-step refinements with $Fo = 0.04$, $Fo = 0.02$ and $Fo = 0.01$ are presented, where $Fo = \alpha \Delta t / Y^2$, α and Y refer to Fourier modulus (dimensionless time), thermal diffusivity and cavity height, respectively. As grid and time-step refinement are effected, the results show that reasonably close agreement is achieved between the current computations and results of Yoo and Viskanta [6].

Also, Fig. 4(c) illustrates a close agreement between predicted (PHASES) and experimental results involving

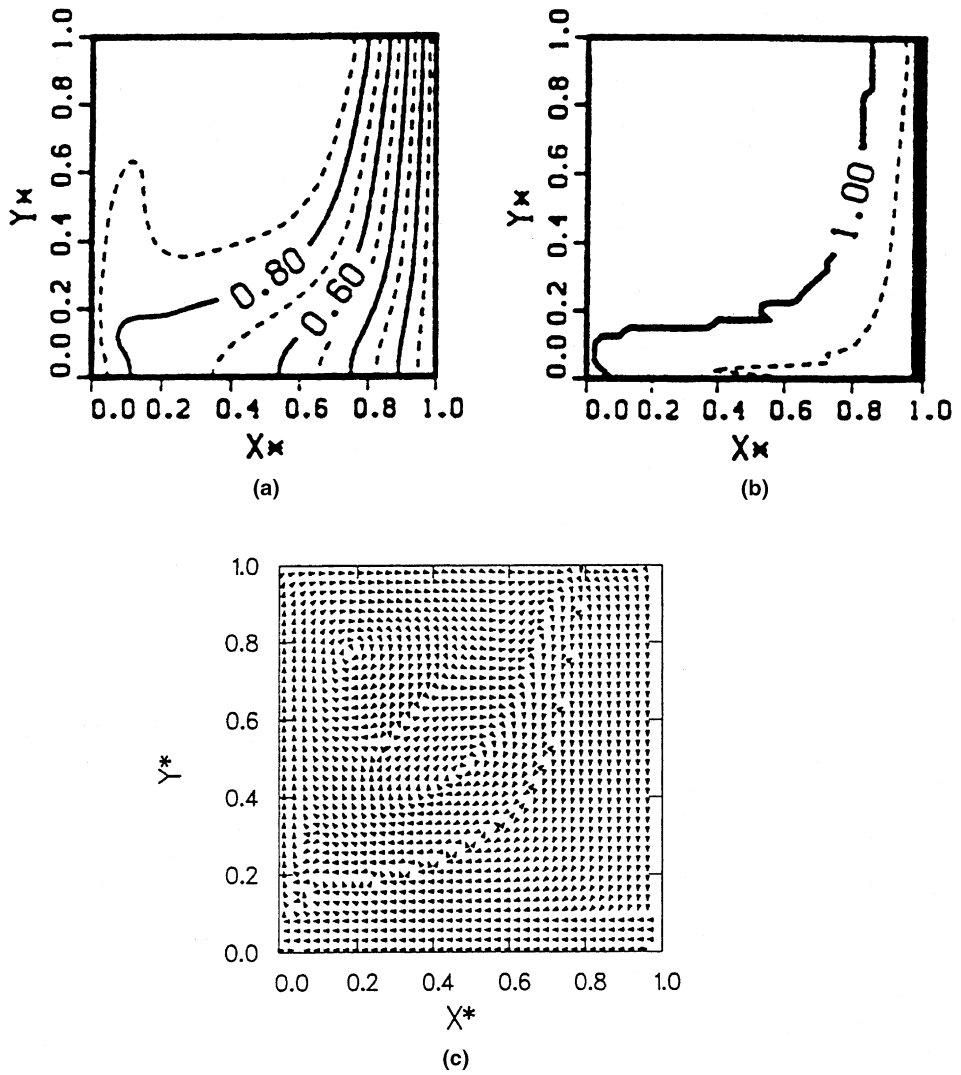

Fig. 3. Problem 1: (a) isotherms, (b) liquid fraction contours and (c) velocity vectors ($t = 1200$ s).

phase interface position (dimensionless), $Y*$ (LIQUIDUS), at $t = 1200$ s. The present permeability model will be interpreted in terms of a heat–entropy analogy whereby thermal irreversibility is used as a weighting factor (i.e. based on entropy production rather than temperature gradient) in establishing the dendritic growth direction and porosity of the solid–liquid mixture. It can be observed that improved accuracy is obtained with the entropy-based permeability in the PHASES algorithm (as compared with isotropic permeabilities adopted by Mehrabian et al. [17] and Blake and Kozeny [18]). The weighting factor between crossflow and axial components of anisotropic permeability is based on the direction of maximum thermal irreversibility because dendritic growth occurs predominantly in this direction. If this weighting is omitted (i.e. previously mentioned isotropic permeabilities [17,18]), Fig. 4(c) shows that the two-phase permeability and rate of interface advance may be over-estimated.

An alternative way of interpreting these results is that entropy is indirectly related to the pressure drop through the interdendritic region. This relationship is analogous to Bernoulli's equation whereby head losses arising from wall friction in viscous pipe flows can be written in terms of entropy produced within the boundary layer. In this way, the magnitude of entropy production is related to frictional head losses in the pipe. In a similar way for interdendritic flow, the component of thermal irreversibility in the direction normal to the local flow direction suggests a corresponding weighting of permeability and pressure drop associated with the crossflow direction. The results in Fig. 4(c) show that a permeability

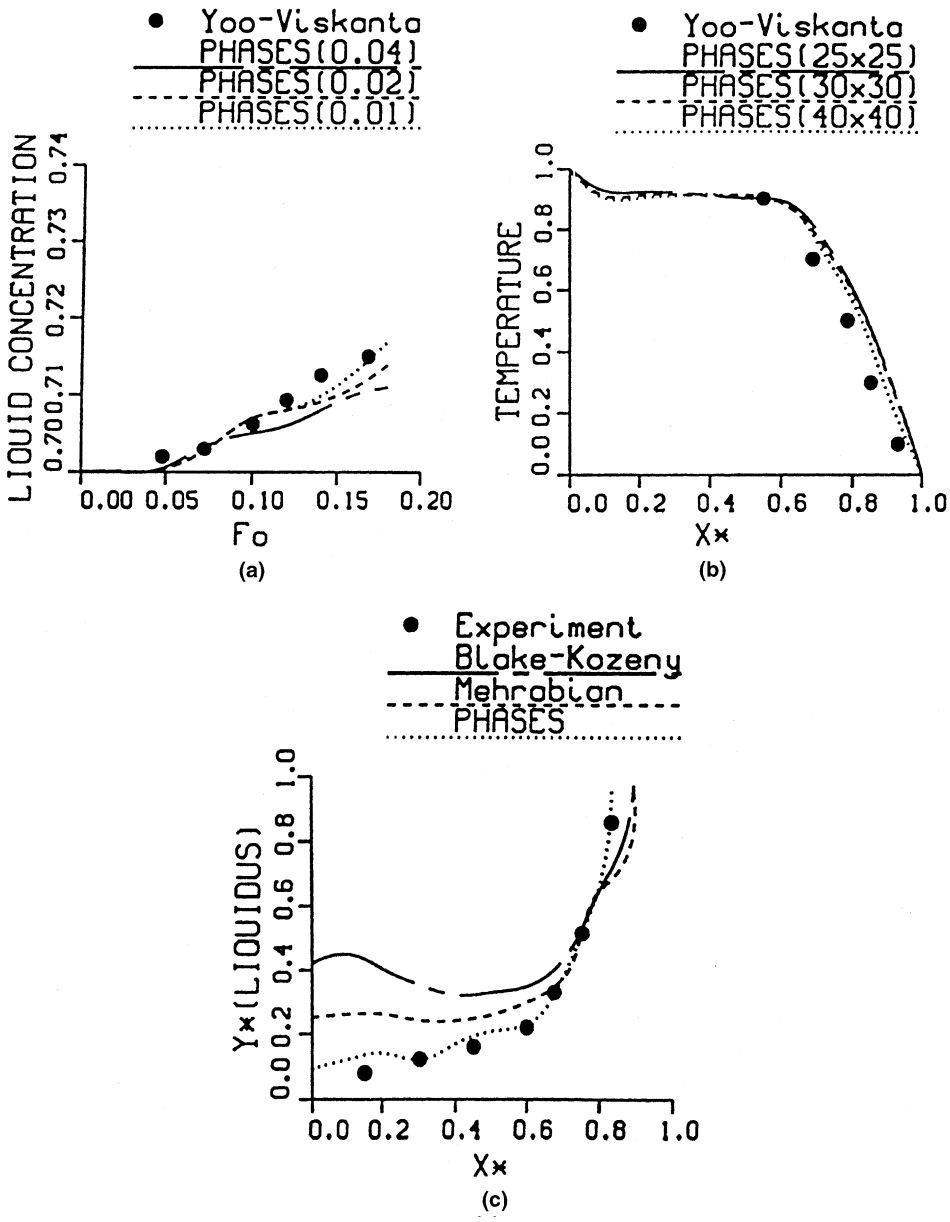

Fig. 4. Problem 1: (a) midpoint liquid concentration, (b) midplane temperature and (c) permeability sensitivity studies.

weighting on crossflow direction can have a significant impact on interface tracking during phase change. The following example provides further experimental data in support of the effectiveness of heat–entropy analogies in phase change problems.

3.2. Problem 2: phase change with double (counter-rotating) convective cells

Numerical and experimental studies of binary mixture solidification in a rectangular enclosure with an insulated top cover were also conducted. A list of initial and boundary conditions for each experiment and test case is given in Table 1. A fixed external rate of cooling was provided by the thermal bath and the resulting transient decline of wall temperatures was recorded. A polynomial fit of these experimental wall measurements is also summarized in Table 1. The coefficients for wall temperature (i.e. a_2, a_1 and a_0) represent a least squares fit of side wall (first row) and base wall (second row) temperature measurements to a second order polynomial for four test cases (described below). In these

Table 1
Experiment boundary/initial conditions

Case	T_0 (K)	T_{bath} (K)	C_0 (H_2O)	a_2	a_1	a_0
1	318	258	0.72	−3.163	20.023	262.88
				−1.554	12.461	262.50
2	318	263	0.68	−4.625	28.921	265.62
				−1.303	13.578	265.25
3	343	263	0.68	−9.453	56.002	267.10
				−1.199	16.728	266.27
4	343	263	0.76	−9.396	54.423	268.53
				−0.987	13.179	265.75

studies, heat–entropy analogies are directed at two-phase permeability, recalescence, coarsening and the overall performance and accuracy of the numerical formulation. In each case, T_0 and C_0 refer to initial temperature and water concentration in the binary mixture, respectively.

3.2.1. Case 1 ($T_0 = 318$ K, $C_0 = 0.72$)

In this case, the phase interface advances rapidly and nearly uniformly across the side and bottom walls during early stages of solidification. Thermal and solutal buoyancy in the liquid region generates two counter-rotating convection cells on the left and right sides of the cavity, respectively (see Fig. 5(a)). Upward transport of crystals by these convection cells and sedimentation of crystals along the vertical midplane creates a growing mushy layer (NH_4Cl dendrites and liquid) along the lower boundary of the domain. A variety of experimental measurements were obtained, including thermocouple measurements and digitally captured images (scanned by pixel intensity thereby delineating phase fraction contours), during solidification (i.e. see Fig. 5(b)). It was observed that crystals along the vertical midplane descended to create an inverted V-shaped sedimentation layer. Due to different sizes and structures of crystals, the descent of various crystals was initiated at different positions. It is anticipated that local thermal conditions, including thermal buoyancy, affected each crystal's trajectory prior to its descent and sedimentation along the lower boundary.

Experimental results for temperature at several interior locations are illustrated in Fig. 6. Thermocouple measurements at positions 6 and 7 experienced a slower rate of temperature decline in comparison to the other locations because of their proximity to the stagnation points of the above-mentioned thermal convection cells. This proximity reduced the rate of convective transport of colder interdendritic fluid to these locations. Other temperatures generally declined in a monotonic fashion except locations 6–8 where local heating, or recalescence, created a temporary thermal fluctuation at $t \approx 370$ s. Similar observations of recalescence have been recorded by other researchers [19]. In addition to similarity with other reported results involving recalescence in aqueous ammonium chloride, it should be noted that repeatable results were obtained in these experiments, based on tests performed at least twice under identical conditions.

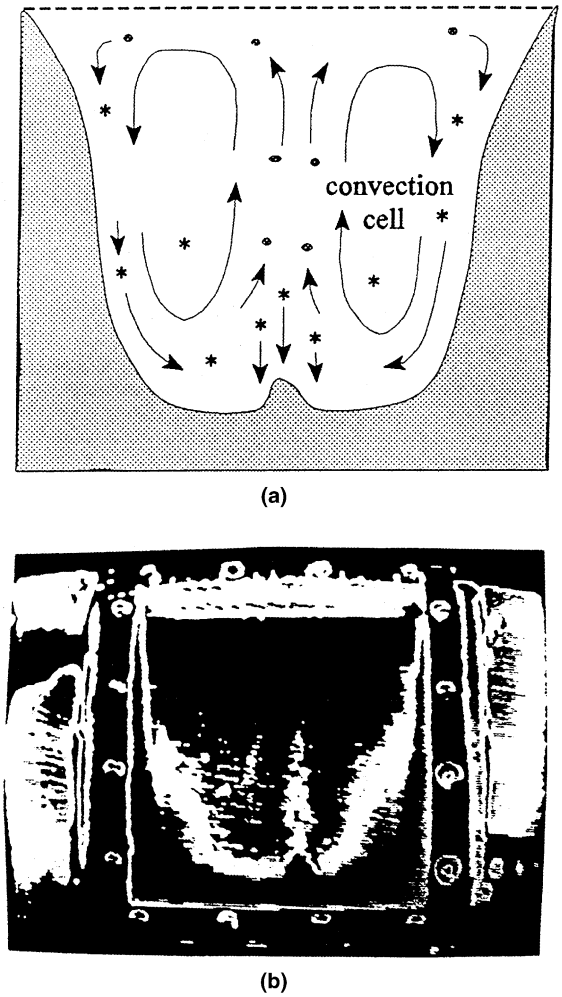

Fig. 5. Problem 2: (a) schematic of convection cells within test section and (b) sample digital imaging result.

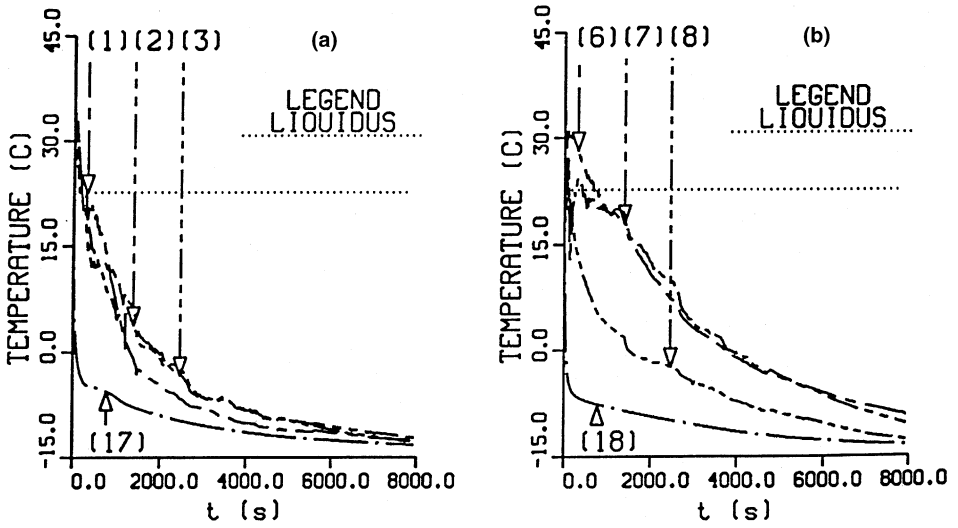

Fig. 6. Problem 2: (a) temperature results (case 1) at locations (a) 1, 2, 3, 17 and (b) 6, 7, 8, 18.

A period of recalescence ($\Delta t > 0$) occurs when the rate of latent heat release within a freezing crystal (or dendrite) exceeds the rate of heat transfer from the solid–liquid mixture around the crystal thereby creating a local heating effect. It can be shown that the rate of latent heat release is dependent on undercooling level, ΔT (i.e. difference between wall temperature and equilibrium freezing temperature), since the undercooling level affects the amount of interfacial energy required for crystals to melt back into the liquid near the phase interface. The duration of recalescence, Δt, can be written in a functional form where $\Delta t \approx A - B/\Delta T^2$. Only points after the intersection between the $\Delta t - \Delta T$ curve and the ΔT axis exhibit recalescence. Recalescence is generally not observed at locations during periods where the thermocouple remains entirely in the liquid phase (i.e. location 5 during early time stages).

It is anticipated that entropy can serve as an effective parameter in understanding and describing various aspects of these thermal processes, including interactions between recalescence and coarsening. In particular, based on consideration of the Gibbs equation and a heat balance on a freezing solid material, another heat–entropy analogy is established, whereby the entropy change of the material with respect to time is related to heat transfer associated with recalescence and/or coarsening. In particular, a high entropy change coincides with a large effective heat transfer coefficient (accounting for simultaneous local cooling and release of latent heat from solidified crystal). Based on this information, the magnitude and duration of recalescence, or coarsening and the propagation of the liquidus interface, can be postulated.

In Fig. 7, the rate of entropy change (Fig. 7(c)), based on corresponding temperature measurements (Fig. 7(a) and (b); $T_{\text{bath}} = 263$ K), is illustrated. In comparison to Fig. 6(a) and (b), it can be observed that a larger magnitude and duration of recalescence is realized in the case with a lower rate of external cooling (or higher temperature of thermal bath). The release of latent heat from newly forming and settling crystals at locations 2, 3 and 4 exceeds this lower rate of cooling, thereby yielding a larger temporary rise of temperature during early stages of solidification. In Fig. 7(c), it can be observed that this temperature rise is accompanied by a positive rate of entropy change (note: experimental approximation of derivative for entropy involves discrete temperature/time differencing yielding positive ds/dt slightly past origin of axis in Fig. 7(c)). The positive rate of entropy change during early stages decreases rapidly and becomes negative after approximately 0.13 h. At this crossing point, the net rate of cooling exceeds the rate of latent heat release. The observed end of recalescence in Fig. 7(a) approximately coincides with the crossing point in Fig. 7(c).

At location 1, the rate of entropy change generally remains negative. It is anticipated that downward buoyant flow reduces the solidification rate at this location as freezing crystals and detached dendrites are transported away by free convective motion near the interface. This downward transport of colder interdendritic fluid provides a brief period whereby the rate of entropy change remains lower at locations 2 and 3, in comparison to location 1, after recalescence (see Fig. 7(c)). Beyond this stage, a generally negative yet increasing rate of entropy change at all locations indicates that external cooling exceeds the release of latent heat from freezing crystals while the test cell approaches a steady state.

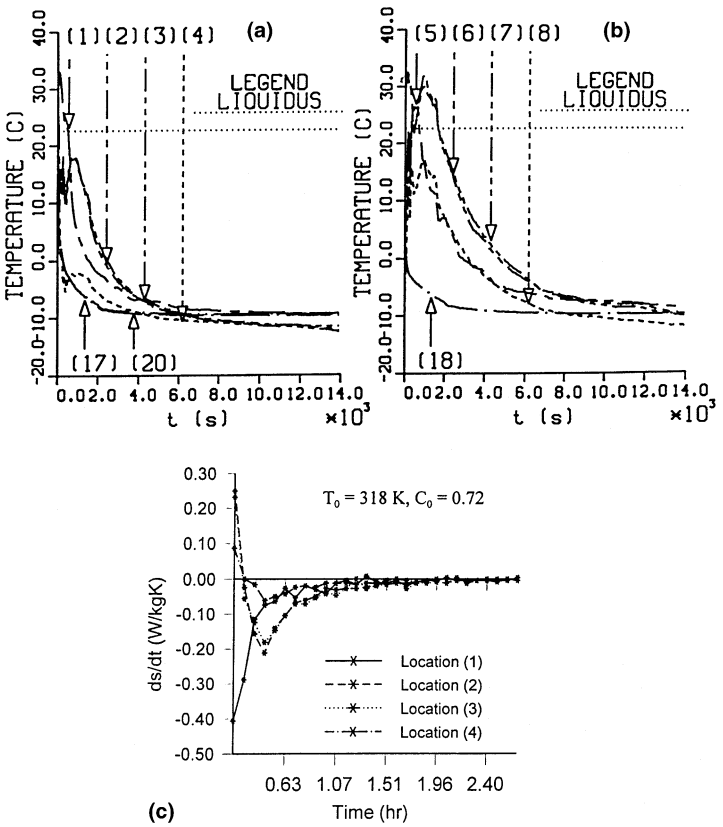

Fig. 7. Problem 2: (a)–(b) temperature and (c) rate of entropy change ($T_b = 263$ K).

3.2.2. Case 2 ($T_0 = 318$ K, $C_0 = 0.68$)

In this case, a lower initial water concentration (in comparison to case 1) yields a higher liquidus temperature and higher initial undercooling level (i.e. wall temperature below liquidus temperature). Unlike the previous case, crystal sedimentation in the form of an inverted V-shaped layer is not observed because the larger initial undercooling level initiates more rapid growth of the stationary mushy layers along the bottom wall relative to deposition of crystals from the convective cells. Initially, the phase interfaces propagate almost uniformly outwards from the walls, but subsequent development of the convective cells leads to more rapid interface growth near the lower boundaries at later stages of solidification.

In addition to experimental studies, numerical simulations were investigated with the heat–entropy analogies. The following conditions and assumptions were adopted in the numerical simulations: (i) two-dimensional flow with stationary solid phase, (ii) uniform concentration and temperature initial conditions and (iii) initially motionless liquid within the test cell. Different mesh configurations (i.e. 400, 625, 900 and 1600 elements) and discrete time steps (i.e. 30 and 60 second steps) were used to establish independence of numerical results with respect to grid spacing and time-step size. Although the time steps may have been larger than timescales of some higher frequency phenomena, such as thermal convection instabilities and crystal free fall time, the implicit time advance provided sufficient resolution of key overall features and trends, including rate of phase interface advance.

In the experimental results (i.e. solid lines in Fig. 8(a)–(c)), a similar pattern of warmer temperatures near the stagnation point of the convective cell arises at location 6 (in comparison to locations 2 and 3). It can be observed from Figs. 6(b) and 8(c) that the initially higher liquid undercooling level in case 2 prolongs the recalescence period at $t \approx 370$ s. In Fig. 8, recalescence is observed where temperatures 2, 3 and 6 attain a local minimum, ascend to a local maximum and then gradually decline. It was observed that these processes coincided closely with the passage of the phase interface past the thermocouple location. After the phase interface passed the specified thermocouple location involving recalescence, the temperature generally declined gradually to a steady-state value.

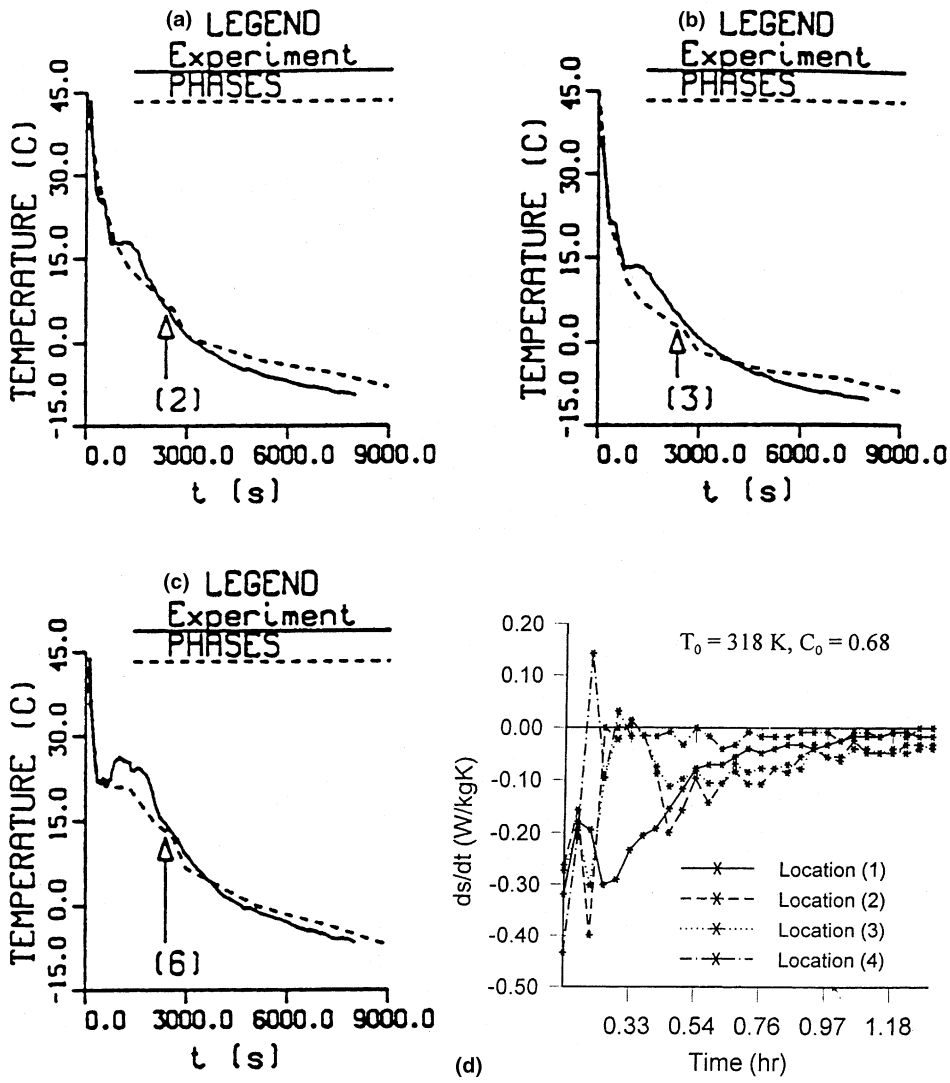

Fig. 8. Problem 2: comparison between numerical and experimental results at locations (a) 2, (b) 3 and (c) 6 and (d) rate of entropy change (case 2).

A comparison between computed and experimental transient results at locations 2, 3 and 6 is also illustrated in Fig. 8(a)–(c). At these locations, both diffusion and convection processes are significant. Comparisons are performed with a grid discretization of 30×30 elements and the entropy-based (anisotropic) permeability is adopted in the two-phase region. It can be observed that the numerical results agree reasonably well with the experimental data. The main trends and features are predicted with reasonable accuracy. Although the numerical results under-estimate the extend of recalescence, such as $t \approx 1000$ s at location 6, a distinct change in profile slope is predicted near this point, thereby indicating the proper rising influence of latent heating in comparison to external (sensible) cooling. Sudden changes in temperature profile slopes typically arise as a result of these simultaneous effects. Also, in coarse grid refinements (as compared to scale of crystal or dendrite size), the release of latent heat is effectively averaged throughout the finite volume thereby diminishing the local magnitude of temperature rise occurring in recalescence. More accuracy can be realized as grid refinement is effected. Furthermore, it will be observed that entropy will provide additional insight into these recalescence processes.

In Fig. 8(d), the results of entropy change corresponding with Fig. 8(a) and (b) are shown. A positive rate of entropy change at location 6, and a smaller positive value at location 2, indicate only a small extent of recalescence at this location (confirmed by measurements

in Fig. 8(b)). Recalescence often promotes repetitive freezing–melting cycles (i.e. oscillations observed in Fig. 8(d)). For example, if a freezing crystal (or detached dendrite arm) releases latent heat and reheats the solid–liquid mixture, it may melt surrounding solid back to a liquid phase. Subsequent solute transfer may undercool the region and once again generate thermal recalescence (i.e. entropy change oscillation between negative and positive value) albeit with a lower magnitude. It is anticipated that heat transfer from the system throughout the process reduces the undercooling levels at each subsequent reheating period. This trend (reduced oscillations at later time stages) is observed in Fig. 8(d).

Thermal irreversibilities arise during recalescence as heat is released by freezing material and transferred to the surrounding liquid or solid. Similarly, irreversibilities arise during coarsening by heat absorption or melting of smaller arms, as well as heat release by growing larger arms. The relative magnitude of these simultaneous effects can be interpreted in terms of magnitude and slope of the entropy change. The magnitude of the maximum entropy change indicates the highest rate of reheating and coarsening, whereas the duration of positive entropy change indicates the approximate time period of recalescence. As the coarsening time increases, more smaller arms disappear while the main dendrite arms grow larger and their spacing increases.

A comparison between experimental and computed results of temperature along the first thermocouple column (i.e. thermocouple locations 1–4) was investigated with 625 (25×25), 900 (30×30) and 1600 (40×40) element grids. The computational results in Fig. 9(a) illustrate good agreement with experimental results as the grid was refined. In addition to good accuracy, the application of phase–temperature iteration rules, based on entropy principles, provides an effective method for obtaining physically realistic and converged phase distributions in an efficient manner.

In Fig. 9(b), predictions of the liquidus interface position with increasing time (or dimensionless time given by Fourier modulus) are presented and compared in terms of various permeability models, including the entropy-based model in PHASES (as described in companion paper), Mehrabian et al. model [17] and Blake et al. model [18]. The interface position is plotted in the horizontal plane at a height of $0.7H$ above the bottom wall, where H refers to the height of the test cell. It can be observed that good agreement between experimental and computational results is achieved and similar results are obtained in all three cases. Recall that more substantial differences between permeability models were obtained in problem (i). Some notable differences with this previous problem, including a lower cooling rate, are present in the current problem. It is expected that less convective transport perpendicular to

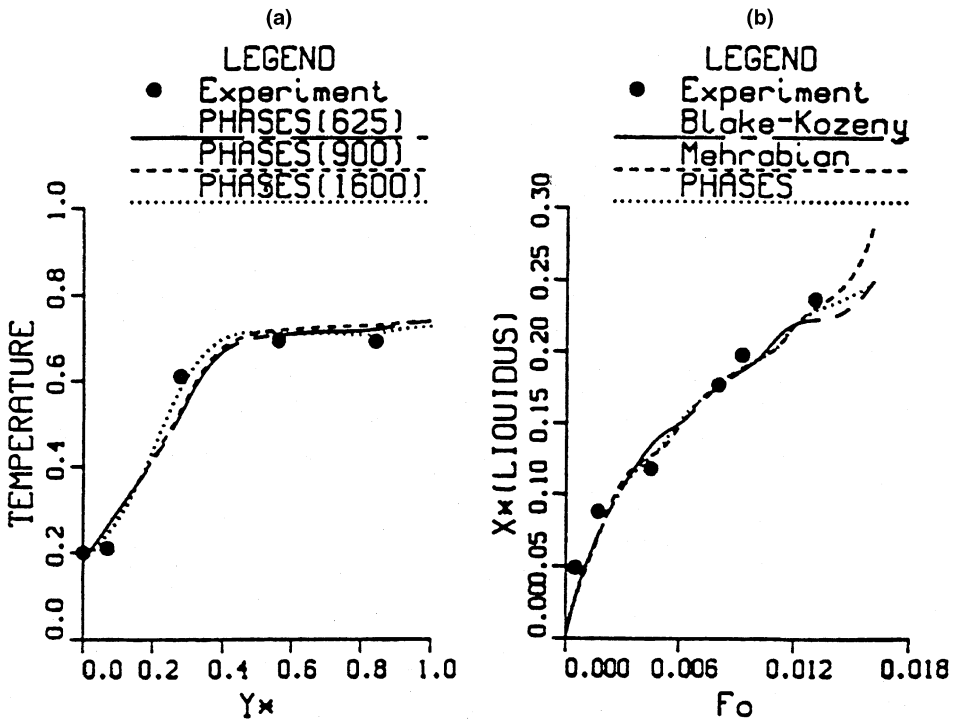

Fig. 9. Problem 2: (a) grid refinement and (b) permeability studies (case 2).

the growth direction of the advancing phase interface would entail a diminished influence of the crossflow component of permeability outlined in the current entropy-based permeability model. In the following two final cases, additional effects of initial liquid temperature and solute concentration will be examined.

3.2.3. Case 3 ($T_0 = 343$ K, $C_0 = 0.68$)

At a higher initial temperature, $T_0 = 343$ K, and water concentration of $C_0 = 0.68$, larger temperature fluctuations during recalescence ($t \approx 0.28$ h) at locations 6–8 were recorded (see Fig. 10(a)). The rate of entropy change for locations 3, 4, 7 and 8 is illustrated in Fig. 10(b). The rate of heating due to release of latent heat is indicated by the magnitude of positive entropy change. Also, coarsening contributes to local reheating since small (secondary) dendrites may become unstable during solidification and melt while the main dendrite arms continue to grow. Since coarsening causes small arms to shrink and/or melt at the expense of growing larger arms, it often accompanies recalescence and so local reheating is often associated with coarsening processes. In Fig. 10(b), positive and negative rates of entropy change provide evidence of contributions arising from local heating (recalescence, coarsening) and external cooling during phase transition.

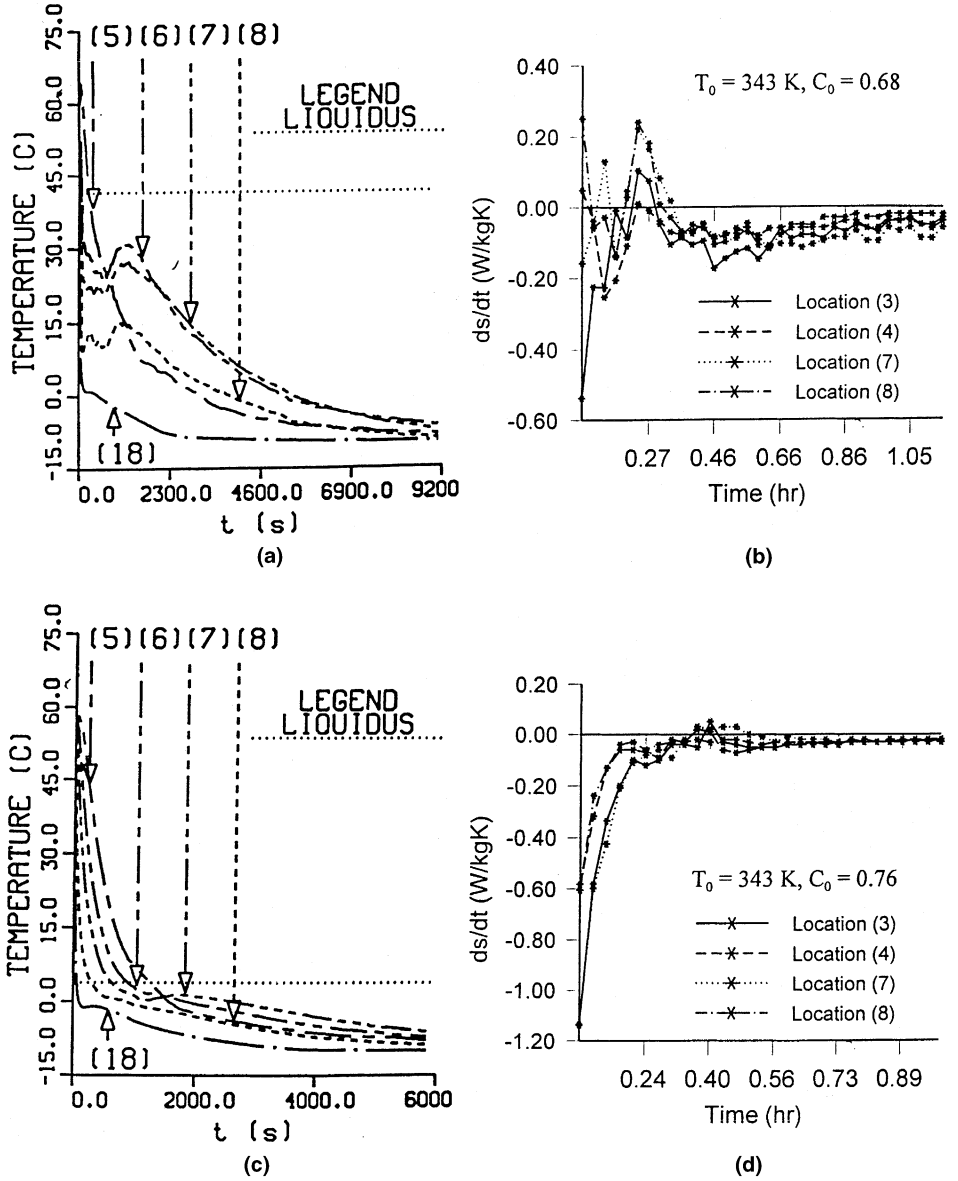

Fig. 10. Problem 2: temperature and rate of entropy change for (a)–(b) case 3 and (c)–(d) case 4.

In the presence of natural convection, the extent of coarsening is affected by the gradient between the interdendritic solutal distribution and the surrounding (incoming or bulk) fluid composition. Solute transferred into the liquid by the main arm diffuses down a solute gradient toward the smaller arm thereby lowering its equilibrium liquidus temperature and melting the smaller arm. However, convective fluid motion may impede this diffusive flow between the dendrite arms and a reduced rate of positive entropy change would indicate a corresponding reduced extent of coarsening (i.e. retaining smaller arm spacings) and recalescence.

3.2.4. Case 4 ($T_0 = 343$ K, $C_0 = 0.76$)

Finally, all conditions of case 3 were repeated with the exception of a higher initial water concentration. In this case, Fig. 10(d) illustrates nominal positive entropy change in comparison to the previous examples. This observation was consistent with measurements of little or no recalescence during solidification at any of the designated thermocouple locations (see Fig. 10(c)). Heat was primarily extracted from the liquid as sensible heat throughout the early stages of solidification as a result of a lower liquidus temperature in this example (as compared with case 3). Beyond this point, only a relatively small temperature difference existed between the liquidus and wall temperatures. As a result, recalescence was not significant in this test case.

In summary, the previous four cases have provided several data points involving undercooling level, ΔT, and period of recalescence, Δt. Thus, a comparison between theoretical predictions of Δt and measured data can be performed. Based on the definition of interface energy, $\sigma \approx \Gamma \Delta s = 10^{-4}$ J/m^2, where Γ refers to the Gibbs–Thompson coefficient, it can be shown that

$$\Delta t \text{ (min)} \approx 0.277 - \frac{17.73}{\Delta T^2}, \tag{1}$$

where Δt must remain positive. Thermophysical property values for the NH_4Cl–H_2O mixture have been adopted in Eq. (1).

Comparisons between experiments and theory for the duration of the first recalescence period at $t \approx 370$ s, in terms of the undercooling level, are shown in Fig. 11. Each set of markers for locations 6 and 7 represents different experiments, including cases 1–3, at the onset of recalescence. The recalescence period, Δt, is defined here as the duration between this onset and the time whereby the temperature declined below a local maximum by 0.5 K. Also, the undercooling level, ΔT, is defined here as the temperature difference between the thermocouple measurement at $t \approx 370$ s and the liquidus temperature at the initial solute concentration. In Fig. 11, it can be observed that reasonable agreement was achieved between the theoretical predictions and the experimental results. High undercooling levels promoted longer recalescence periods whereas lower undercooling levels (i.e. $\Delta T < 8$ K) initiated phase transition at a rate which released latent heat slower than the rate of heat transfer from the crystal or detached dendrites (i.e. recalescence not observed in some cases). These trends in recalescence duration with respect to undercooling level can also be observed in terms of the positive entropy change results (i.e. Figs. 7(c), 8(d), 10(a) and (b)).

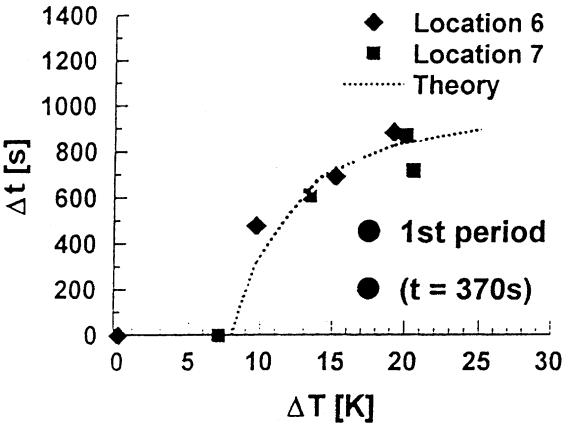

Fig. 11. Problem 2: summary of thermal recalescence results.

4. Conclusions

Numerical and experimental studies of solid–liquid phase change with heat–entropy analogies have been presented. An entropy-based approach is adopted for stability of computations and efficient numerical iterations in the finite element-volume numerical model. In solidification problems with binary mixtures, a permeability model with an entropy-based weighting factor is shown to provide an effective model of phase interactions in the momentum equations. Furthermore, recalescence and coarsening processes are investigated through analogies between heat and entropy processes. In particular, the onset and duration of thermal recalescence was characterized by local rates of entropy change. Good agreement between computational predictions and experimental results was achieved in the current studies. In summary, it is anticipated that further advances in understanding of interfacial processes during phase change can be obtained through analogies between heat and entropy processes.

Acknowledgements

The work in this paper was supported, in part, by a research grant from the Natural Sciences and Engineering Research Council of Canada to the author.

Appendix A. Experimental uncertainties

A.1. Three-dimensional flow field effects within the test cell were negligible

A net static force balance on the fluid within the test cell involves a balance between buoyancy and wall friction forces. If the front and back wall friction forces are comparable to the side friction forces, then the internal flow field may be distorted due to these end effects even though it may appear to be a two-dimensional flow.

Differentiating the velocity field in the similarity profile for laminar free convection flow [20] and then evaluating functional quantities at the wall ($\eta = 0$), we obtain the following ratio of front and back frictional forces to total cell frictional forces:

$$\frac{F_{\mathrm{f-b}}}{\sum F_{\mathrm{s,f-b}}} \approx \frac{2HW}{2HW + r(2HD + WD)}$$

$$\text{where } r = \frac{\mu \frac{\partial u}{\partial y}|_{W,\mathrm{s}}}{\mu \frac{\partial u}{\partial y}|_{W,\mathrm{f}}} = \left(\frac{\Delta T_{\mathrm{s}}}{\Delta T_{\mathrm{a}}}\right)^{3/4}. \tag{A.1}$$

In the above equations, H, W, D and the subscripts s, f–b and a represent cell height, width, depth and side, front–back and ambient, respectively. For representative flow conditions, $T_0 \approx 313$ K, $T_{\mathrm{s}} \approx 253$ K and the frictional force ratio becomes approximately 10.0% in the worst case (initial condition) scenario. In practice, this ratio will be much smaller as solidification proceeds along the side and bottom walls. As a result, the fluid flow was considered approximately two-dimensional in the centre measurement plane of the test cell.

A.2. The plexiglass covers of the test cell were approximately adiabatic

Considering an identical temperature difference across the side brass (sb) wall and front plexiglass (fp) wall, as well as conduction heat transfer across each wall of thickness t, and cross-sectional area A, then the ratio of heat flows between the front and side walls, ω, may be expressed as a ratio of thermal resistances [20], in the following manner:

$$\omega = \frac{t_{\mathrm{sb}}/k_{\mathrm{sb}}A}{t_{\mathrm{fp1}}/k_{\mathrm{fp}}A + t_{\mathrm{a}}/k_{\mathrm{a}}A + t_{\mathrm{fp2}}/k_{\mathrm{fp}}A}. \tag{A.2}$$

Considering equivalent areas, and actual thicknesses, $t_{\mathrm{sb}} = 1.59$ mm, $t_{\mathrm{fp1}} = t_a = 3.18$ mm and $t_{\mathrm{fp2}} = 1.59$ mm, then $\omega \approx 0.0001\%$, i.e., heat losses through the window gap are negligible. Within the air gap, $Ra_{\mathrm{L}} \approx 1700 < Ra_{\mathrm{crit}}$; the effects of natural convection within the internal cavity are considered negligible as compared with conduction heat transfer.

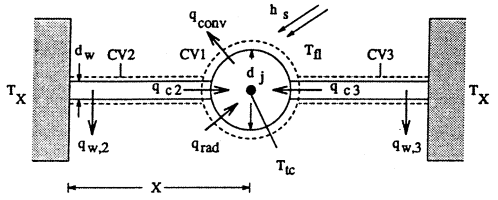

Fig. 12. Thermocouple junction.

A.3. Thermocouple errors due to convection and conduction heat losses down the thermocouple wires were negligible

A thermocouple error analysis revealed the magnitude of the heat losses from the thermocouple junction (see Fig. 12). From an energy balance on the junction (CV1)

$$q_{\mathrm{conv}} = q_{\mathrm{Cu}} + q_{\mathrm{Co}}, \tag{A.3}$$

where q_{conv}, q_{Cu} and q_{Co} represent convection and conduction (copper and constantan wires) heat losses, respectively. Radiation exchange with the walls has been neglected. Convective heat transfer to the thermocouple junction was estimated by a free convection correlation from a sphere [20]

$$q_{\mathrm{conv}} = \left(2.0 + \frac{0.59Ra_{\mathrm{d}}^{0.25}}{[1 + (0.47/Pr)^{0.5625}]^{0.444}}\right) A_{\mathrm{tc}}(T_{\mathrm{fl}} - T_{\mathrm{tc}})$$
$$\equiv \gamma(T_{\mathrm{fl}} - T_{\mathrm{tc}}), \tag{A.4}$$

where the subscripts tc and fl refer to thermocouple and fluid, respectively. A fin analysis (CV2 and CV3) [20] was then employed for the conduction heat losses, i.e.,

$$q_{\mathrm{Cu}} = (mk_{\mathrm{Cu}}A)[(T_{\mathrm{tc}} - T_0)\coth(mX) - (T_X - T_0)\operatorname{csch}(mX)], \tag{A.5}$$

where $m = \sqrt{hP/kA}$ and h and P refer to the local convection coefficient and wire perimeter, respectively. Defining $T_{\mathrm{tc}} = T_{\mathrm{fl}} + \epsilon$ (K) and combining Eqs. (A.3)–(A.5) yields a single equation for ϵ:

$$f(\epsilon) \equiv \gamma\epsilon + \sum_{i=\mathrm{Cu,Co}} \{mk_iA[(T_{\mathrm{fl}} + \epsilon - T_0)\coth(mX) - (T_X - T_0)\operatorname{csch}(mX)]\} = 0. \tag{A.6}$$

The solution of Eq. (A.6) by Newton's method, i.e., $f(\epsilon) = 0$ ($d_{\mathrm{w}} = 0.51$ mm, $Ra = 1.0 \times 10^6$, $Pr = 9.025$, $T_{\mathrm{fl}} = 293$ K and $T_0 = 293$ K), yielded $\epsilon/T_{\mathrm{fl}} \ll 1$. As a result, the thermocouple errors were considered negligible.

References

[1] Y. Hayashi, T. Komori, Investigation of freezing of salt solutions in cells, J. Heat Transfer 101 (1979) 459–464.

[2] J. Szekely, A. Jassal, An experimental and analytical study of the solidification of a binary dendritic solution, Metallur. Trans. 9b (1978) 389–398.
[3] C. Beckermann, R. Viskanta, An experimental study of melting of binary mixtures with double-diffusive convection in the liquid, Exp. Therm. Fluid Sci. 2 (1989) 17–26.
[4] J. Cahoon, M. Chaturvedi, K. Tandon, The unidirectional solidification of Al–4 Wt Pct Cu ingots in a microgravity, Metallur. Mater. Trans. 29a (1998) 1101–1111.
[5] G.F. Naterer, Simultaneous pressure–velocity coupling in the two-phase zone for solidification shrinkage in an open cavity, Modelling Simulat. Mater. Sci. Eng. 5 (6) (1997) 595–613.
[6] H. Yoo, R. Viskanta, Effect of anisotropic permeability on the transport process during solidification of a binary mixture, Int. J. Heat Mass Transfer 35 (10) (1992) 2335–2346.
[7] T.W. Clyne, W. Kurz, Solute redistribution during solidification with rapid solid state diffusion, Metallur. Trans. A 12 (1981) 965.
[8] V.R. Voller, D. Brent, The modelling of heat, mass and solute transport in solidification systems, Int. J. Heat Mass Transfer 32 (9) (1989) 1719–1731.
[9] G.F. Naterer, G.E. Schneider, Phases model of binary constituent solid–liquid phase transition – Part 2. Applications, Numer. Heat Transfer B 28 (2) (1995) 127–137.
[10] G.F. Naterer, Numerical and experimental techniques for binary solid–liquid phase transition, Ph.D. Thesis, Department of Mechanical Engineering, University of Waterloo, Canada, 1995 (Chapter 4).
[11] R. Burton, G. Yang, Z.F. Dong, M.A. Ebadian, An experimental investigation of the solidification process in a V-shaped sump, Int. J. Heat Mass Transfer 38 (13) (1995) 2383–2393.
[12] G.F. Naterer, Predictive entropy based correction of phase change computations with fluid flow – Part 1. Second law formulation, Numer. Heat Transfer B 37 (4) (2000) 393–414.
[13] G.F. Naterer, Predictive entropy based correction of phase change computations with fluid clow – Part 2. Application problems, Numer. Heat Transfer B 37 (4) (2000) 415–436.
[14] G.F. Naterer, Constructing an entropy-stable upwind scheme for compressible fluid flow computations, AIAA J. 37 (3) (1999) 303–312.
[15] M.J. Vesligaj, C.H. Amon, Transient thermal management of temperature fluctuations during time varying workloads on portable electronics, IEEE Trans. Components Packaging Technol. 22 (4) (1999) 541–550.
[16] D. Miller, Chem. Rev. 60 (1) (1960) 15–29.
[17] R. Mehrabian, M. Keane, M.C. Flemings, Interdendritic fluid flow and macrosegregation: influence of gravity, Metallur. Trans. 1 (1970) 1209–1220.
[18] R. Bird, W. Stewart, E. Lightfoot, Transport Phenomena, Wiley, New York, 1960.
[19] M.S. Christenson, W.D. Bennon, F.P. Incropera, Solidification of and aqueous ammonium chloride solution in a rectangular cavity – II. Comparison of predicted and measured results, Int. J. Heat Mass Transfer 32 (1989) 69–79.
[20] F.P. Incropera, D.P. DeWitt, Fundamentals of Heat and Mass Transfer, fourth ed., Wiley, New York, 1996 (Chapter 9).